

# DSCA: A Dual-Stream Network with Cross-Attention on Whole-Slide Image Pyramids for Cancer Prognosis <sup>★</sup>

Pei Liu<sup>a</sup>, Bo Fu<sup>a</sup>, Feng Ye<sup>b</sup>, Rui Yang<sup>a</sup>, Luping Ji<sup>a,\*</sup>

<sup>a</sup>School of Computer Science and Engineering, University of Electronic Science and Technology of China, Xiyuan Ave, Chengdu, 611731, Sichuan, China

<sup>b</sup>Institute of Clinical Pathology, West China Hospital, Sichuan University, Guo Xue Xiang, Chengdu, 610041, Sichuan, China

## Abstract

The cancer prognosis on gigapixel Whole-Slide Images (WSIs) has always been a challenging task. To further enhance WSI visual representations, existing methods have explored image pyramids, instead of single-resolution images, in WSIs. Despite this, they still face two major problems: high computational cost and the unnoticed semantical gap in multi-resolution feature fusion. To tackle these problems, this paper proposes to efficiently exploit WSI pyramids from a new perspective, the dual-stream network with cross-attention (DSCA). Our key idea is to utilize two sub-streams to process the WSI patches with two resolutions, where a square pooling is devised in a high-resolution stream to significantly reduce computational costs, and a cross-attention-based method is proposed to properly handle the fusion of dual-stream features. We validate our DSCA on three publicly-available datasets with a total number of 3,101 WSIs from 1,911 patients. Our experiments and ablation studies verify that (i) the proposed DSCA could outperform existing state-of-the-art methods in cancer prognosis, by an average C-Index improvement of around 4.6%; (ii) our DSCA network is more efficient in computation—it has more learnable parameters (6.31M vs. 860.18K) but less computational costs (2.51G vs. 4.94G), compared to a typical existing multi-resolution network. (iii) the key components of DSCA, dual-stream and cross-attention, indeed contribute to our model’s performance, gaining an average C-Index rise of around 2.0% while maintaining a relatively-small computational load. Our DSCA could serve as an alternative and effective tool for WSI-based cancer prognosis. Our source code is available at <https://github.com/liupeil101/DSCA>.

**Keywords:** Whole-Slide Image, Computational Pathology, Cancer Prognosis, Survival Analysis, Multiple Instance Learning

## 1. Introduction

Cancer prognosis typically answers the question of how the disease will develop for patients. It can be affected by various factors such as primary site, tumor grade, and treatment response (De Boer et al., 2009). Among these factors, some tumor-related ones can be uncovered by the histopathology Whole-Slide Image (WSI) from a high-end microscope (Zarella et al., 2018; Bankhead et al., 2017). Thereby, WSIs are often utilized by doctors to assess patients’ diseases and further make clinical decisions. Different from natural images, medical WSIs have extremely-high resolution, usually with gigapixels. And the WSIs at different magnifications present distinct microscopic views (Zarella et al., 2018; Chen et al., 2022). These views can exhibit rich pathological entities, from tissue phenotypes (5×) to cellular organization (20×), and even to individual cells (40×), as shown in Figure 1.

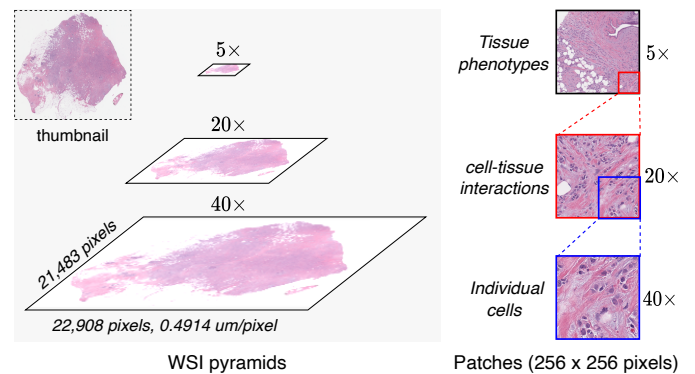


Figure 1: Histopathology whole-slide image pyramids and their respective image patches.

Due to the gigapixel inherent in WSIs, a computational modeling paradigm (Chen et al., 2022) is usually decomposed into (i) slicing images into a myriad of small image patches and (ii) modeling these patches by using bag-level multiple instance learning (MIL) methods. In the early years, most works of modeling WSIs for cancer prognosis focus on single-resolution images (Zhu et al., 2017; Li et al., 2018; Di et al., 2020; Yao et al., 2020; Shao et al., 2021a; Chen et al., 2021; Huang et al., 2021). From a unified perspective, these works aim at making patch information flow within a specified structure to learn patch de-

<sup>★</sup>This work is supported by the National Natural Science Foundation of China (NSFC) under Grant No. 61972072, partly by Sichuan Science and Technology Program under Grant No. 2021YFS0071 and 2021YFS0236, West China Hospital-UESTC Medical & industrial integration cross talent training fund ZYGX2022YGRH015, and the West China Hospital 1.3.5 project for disciplines of excellence under Grant No. ZYJC21035.

\*Corresponding author: L. Ji (jiluping@uestc.edu.cn).

Email addresses: yuukilp@163.com (Pei Liu), fubo@uestc.edu.cn (Bo Fu), fengye@scu.edu.cn (Feng Ye), yang19981125@126.com (Rui Yang), jiluping@uestc.edu.cn (Luping Ji)

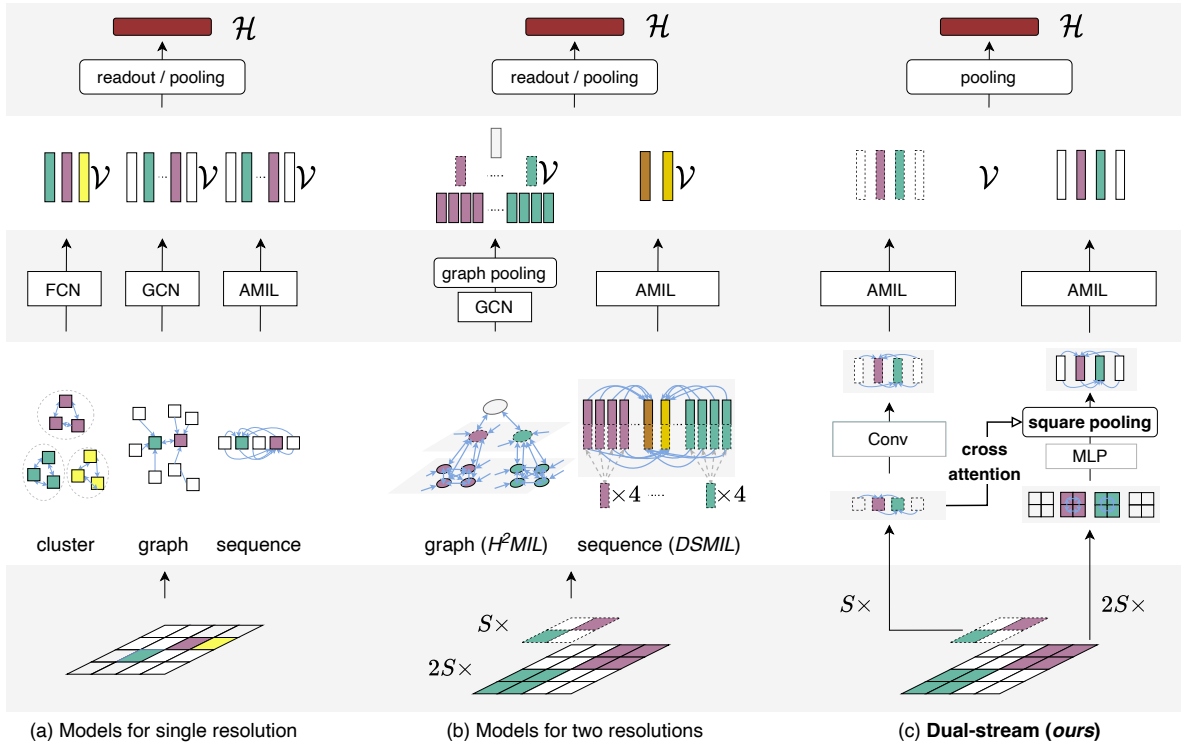


Figure 2: Comparison of architectures. Colored patches are taken as examples to illustrate how networks process them. The blue line indicates patch aggregation flow. Dashed ones are low-resolution items.  $S$  denotes image resolution.  $\mathcal{V}$  is the set of patches after dependency learning.  $\mathcal{H}$  denotes WSI-level representation. AMIL means attention-based MIL network and MLP represents multi-layer perceptron. The details of (a) and (b) are available in Section 2. The proposed architecture (c) is elaborated in Figure 3.

dependencies, and then outputting new patch embeddings to derive effective WSI representations, as shown in Figure 2(a). For example, Li *et al.* originally adopt graph to describe patches (Li *et al.*, 2018). And they train a graph convolution network (GCN) to learn patch embeddings and WSI representations. Afterward, other patch structures (*e.g.*, cluster and sequence) and networks (*e.g.*, fully-connected networks and attention-based MIL networks) are further tried for WSI-based cancer prognosis (Yao *et al.*, 2020; Shao *et al.*, 2021a; Huang *et al.*, 2021), as illustrated in Figure 2(a). However, the single-resolution nature of these schemes greatly hinders models from fully utilizing inherent WSI pyramids (see Figure 1) for a more accurate cancer prognosis.

Motivated by pathologist’s experience (examining WSIs from the region of interest to tumor localization) (Zarella *et al.*, 2018), as well as the idea of hierarchical vision representation (Adelson *et al.*, 1984), WSI-based methods have gradually evolved into multi-resolution from single-resolution over recent years (Pati *et al.*, 2020; Li *et al.*, 2021a; Hou *et al.*, 2022; Chen *et al.*, 2022). DSMIL (Li *et al.*, 2021a) is a representative multi-resolution scheme. It tries to utilize WSI pyramids by simply concatenating the patch features at different magnifications, as illustrated in Figure 2(b). By contrast,  $H^2MIL$  (Hou *et al.*, 2022) adopts a multi-layer graph to model multi-resolution patches. It especially builds cross-layer connections (or edges) for cross-resolution patches to integrate and exploit hierarchical features, as shown in Figure 2(b). Although

these multi-resolution schemes have demonstrated better results than single-resolution ones, the way of *explicitly* using high-resolution patches throughout patch embedding learning is not efficient enough. Because there is usually an enormous amount of patches in high-resolution WSIs, whose number may be up to 10,000 at 20 $\times$  magnification. In addition, from the perspective of multi-scale feature fusion (Lin *et al.*, 2017; Tan *et al.*, 2020; Zhang *et al.*, 2020), existing schemes have not paid enough attention to the intrinsic semantical gap in different resolution patches, but are restricted to simple concatenating (DSMIL) or direct message passing ( $H^2MIL$ ) for multi-resolution feature fusion.

To tackle the problems analyzed above, we propose an alternative scheme based on a different idea, a dual-stream network with cross-attention (DSCA), as shown in Figure 2(c). This scheme is inspired by modern feature pyramid networks (Lin *et al.*, 2017; Tan *et al.*, 2020; Zhang *et al.*, 2020; Wang *et al.*, 2021). Briefly, our multi-resolution scheme consists of two vital components: dual-stream and cross-attention. The former is utilized to process low- and high-resolution patches respectively, so as to efficiently learn hierarchical WSI representation; the latter handles the potential semantical gap in dual-resolution features. Specifically, in the high-resolution stream, we devise a square pooling layer to largely decrease the number of high-resolution patches, exploiting fine-grained features efficiently. Furthermore, this square pooling is implemented by a cross-attention-based method that pools high-resolution patches un-

der the guidance of a global low-resolution one. Notably, our DSCA could be easily extended to multi-stream to model multi-resolution WSIs when its computational cost is feasible.

We summarize our main contributions as follows:

(1) A dual-stream network with cross-attention (DSCA) is proposed to learn hierarchical representations from WSI pyramids for cancer prognosis. It has three highlights:

- We propose a novel scheme, a dual-stream network with cross-attention, to fully utilize image pyramids for enhancing the visual representation of WSIs. This scheme’s key idea is quite distinct from other WSI-based multi-resolution ones.
- A square pooling layer is devised to significantly decrease the number of high-resolution patches, thus largely reducing the computational cost in network training. It serves as a critical component for computation efficiency.
- A cross-attention-based pooling method is proposed to pool high-resolution patches under the guidance of a global low-resolution one. It could effectively handle the potential semantical gap between high- and low-resolution features, making the fusion of dual-stream features smoother. It is a specific implementation of square pooling leveraged to enhance hierarchical representation for better prediction performance.

(2) We carry out extensive experiments on three publicly-available WSI datasets and empirically prove that the proposed DSCA could often outperform existing state-of-the-art methods in cancer prognosis owing to its dual-stream architecture with cross-attention.

## 2. Related work

This section will introduce (i) the image and feature pyramids in computer vision, (ii) traditional multiple instance learning (MIL) framework, and (iii) MIL-based WSI representation learning. To better compare the existing works related to WSI representation learning, we summarize representative ones and exhibit them in Table 1.

### 2.1. Image and feature pyramid

In computer vision, feature pyramids also refer to multi-scale or hierarchical features. It can be extracted from images to enhance visual representation. Traditional computer vision methods usually get feature pyramids from image pyramids by scaling original images (Adelson et al., 1984). By contrast, modern deep learning methods typically achieve this purpose by only using ConvNets (Simonyan & Zisserman, 2014; He et al., 2016), not directly relying on image pyramids. Because ConvNets can produce feature maps with multi-scale receptive fields, showing a pyramidal shape. And these feature maps are inherent with hierarchical and semantically-distinct information (Zeiler & Fergus, 2014).

In order to effectively exploit the feature pyramids derived from the nature of deep neural networks, a typical solution (Lin

et al., 2017; Tan et al., 2020; Zhang et al., 2020) is to make multi-scale feature maps in the same scale via downsampling or upsampling operators, and then to add these feature maps for a multi-scale feature fusion. However, as the approaches that use feature pyramids similarly, existing multi-resolution schemes have not paid enough attention on how to better fuse multi-resolution patch features in WSI representation learning, but are restricted to a simple feature concatenating (Li et al., 2021a) or a direct message (feature) passing between graph nodes (Hou et al., 2022).

### 2.2. Multiple instance learning

Multiple Instance Learning (MIL) is a weakly-supervised learning framework (Dietterich et al., 1997; Carbonneau et al., 2018). In MIL settings, the dataset can be written by

$$T = \{(X_i, y_i)\}_{i=1}^{i=N}, X_i = \{I_i^{(j)}\}_{j=1}^{j=n_i}, \quad (1)$$

where  $X_i$  denotes a bag sample,  $y_i$  is the label of  $X_i$ , and  $I_i^{(j)}$  is the  $j$ -th instance of  $X_i$ . A bag sample contains multiple instances and only bag labels are available. Traditional MIL approaches can be divided into bag-level MIL and instance-level MIL (Wang et al., 2018). And the former aims to learn bag-level representation.

In WSI modeling, WSIs and patches can be viewed as bags and instances, respectively. Thus, most WSI-based approaches are also cast as MIL. Moreover, these approaches belong to bag-level MIL, focusing on learning WSI-level representation. We will review them in the following part.

### 2.3. WSI-level representation learning

#### 2.3.1. Single-resolution

The schemes in this class usually use the WSIs at 20× magnification, since this resolution is enough to capture cell-tissue interactions and its computational cost is reasonable. To learn WSI-level representation, these schemes often learn patch dependencies at first and then aggregate all patch embeddings into WSI-level features, as shown in Figure 2(a). In patch dependency learning, patches are often organized as clusters, graphs, or sequences (referring to those patches without any specified structures). (i) Cluster-based schemes (Zhu et al., 2017; Yao et al., 2020; Shao et al., 2021a) often adopt patch similarity for clustering and then learn patch dependencies in each cluster using fully-connected networks. (ii) Graph-based schemes (Li et al., 2018; Di et al., 2020; Chen et al., 2021) turn to adopt graph to construct patch dependences. They pass or aggregate patch-level features along graph edges using GCNs. (iii) Sequence-based schemes (Huang et al., 2021; Li et al., 2021b; Shao et al., 2021b) don’t limit any structure for patches, *i.e.*, their models are structure-free. They learn all possible dependencies via attention-based networks, *e.g.*, Transformer (Vaswani et al., 2017), Attention-MIL (Ilse et al., 2018), or Vision Transformer (ViT) (Dosovitskiy et al., 2021). WSI-level representation is usually obtained from patch-level embeddings by a global pooling operator at the end. However, the single-resolution nature of these various schemes could hinder models from fully utilizing WSI pyramids (see Figure 1).

Table 1: Works related to WSI classification or cancer prognosis.

Structure	Method	Task	Pyramid	Network	Highlights
cluster	WSISA (Zhu et al., 2017)	prognosis		FCN	the first deep learning model
	DeepAttnMISL (Yao et al., 2020)	prognosis		FCN	cluster attention
	BDOCOX (Shao et al., 2021a)	prognosis		FCN	pseudo-bag; ranking loss
graph	DeepGraphSurv (Li et al., 2018)	prognosis		SpectralGCN	the first graph-based model
	RankSurv (Di et al., 2020)	prognosis		HyperGCN	hyper-graph network
	PatchGCN (Chen et al., 2021)	prognosis		GCN	regional graph
	H <sup>2</sup> MIL (Hou et al., 2022)	classification	✓	GCN	heterogeneous graph
sequence	SeTranSurv (Huang et al., 2021)	prognosis		Transformer	Transformer MIL
	DT-MIL (Li et al., 2021b)	classification		Transformer	deformable Transformer MIL
	TransMIL (Shao et al., 2021b)	classification		Transformer	CNN positional encoding
	DSMIL (Li et al., 2021a)	classification	✓	Attention-MIL	the first patch pyramid model
	DTFD-MIL (Zhang et al., 2022)	classification		Attention-MIL	CAM inspired MIL aggregation
	HIPT (Chen et al., 2022)	both	✓	Transformer	self-supervised pre-training

### 2.3.2. Multi-resolution

Both DSMIL and H<sup>2</sup>MIL belong to this class, as shown in Figure 2(b). In sequence-based DSMIL, multi-resolution features are simply concatenated for patch dependency learning. And only those selected key patches could have connections with other patches. In graph-based H<sup>2</sup>MIL (Hou et al., 2022), the edges between low- and high-resolution patches are built additionally, compared to those graph-based single-resolution models. However, these cross-resolution edges only can be used to transfer patch features directly, and the intrinsic semantical gap between different resolution patches remains when calculating WSI-level features by global patch pooling. Most recently, the HIPT (Chen et al., 2022), built upon ViT, also utilizes WSI pyramids and has achieved promising results on WSI classification and prognosis, but it focuses on studying a hierarchical self-supervised pre-training strategy for WSIs.

It is worth noting that, among the approaches exhibited in Table 1, DSMIL and DTFD-MIL *only can be used for classification*, because DSMIL selects key patches using class scores and DTFD-MIL relies on class-specific CAMs (Zhou et al., 2016). In addition, as the two most popular tasks on WSIs—classification and prognosis, there are many differences between them. For example, identifying a specific tumor stage or subtype is usually the end of most classification-oriented models (Moitra & Mandal, 2020; Houssein et al., 2021; Zeiser et al., 2021; Pati et al., 2022; Ding et al., 2022). Although tumor stage and subtype are well-known prognostic factors, more evidence in WSIs, such as the certain traits of cancer cells and the tumor surrounding micro-environmental cues (Bremnes et al., 2011; Yu et al., 2016), is often required to gather by cancer prognosis models (Shao et al., 2019; Skrede et al., 2020; Liu et al., 2022). This means that actual prognostic patterns may be more complex in patients’ WSIs. And these factors can vary across cancer types and individuals due to tumor heterogeneity and individual diversity (Fu et al., 2019; Alizadeh et al., 2015), thus leaving the cancer prognosis on WSIs as a more difficult task. We will discuss more through empirical experiments.

## 3. Methodology

Our DSCA architecture (see Figure 3) has four key components: 1) token embedding layer, 2) dependency learning layer, 3) dual-stream fusion, and 4) prediction layer, from input to output. The first two components are dual-stream versions, as shown in Figure 3(b). The network architecture of two sub-streams roughly follows the philosophy of ViT (Dosovitskiy et al., 2021).

### 3.1. Problem formulation

#### 3.1.1. Dataset

We denote our dataset by

$$T = \{(\mathcal{P}_i, t_i, c_i)\}_{i=1}^{i=N}, \mathcal{P}_i = \{p_i^{(j)}\}_{j=1}^{j=m_i}, \quad (2)$$

where  $\mathcal{P}_i$ ,  $t_i$ , and  $c_i$  are the WSI material, follow-up time, and censorship status of the  $i$ -th patient, respectively.  $p_i^{(j)}$  denotes the  $j$ -th patch data in  $\mathcal{P}_i$ . And  $m_i$  is the total number of patches in  $\mathcal{P}_i$ , which could be different across patients. Throughout the paper, the word *patch* means the *image patch* sliced from WSIs, and the word *token* means the *feature vector* corresponding to that patch.

#### 3.1.2. Dual-resolution

The dual-resolution patches from WSI pyramids are used for our DSCA network. Without loss of generality, we denote the magnification of patches with a lower resolution by  $S\times$ , and that with higher resolution by  $\lambda S\times$ , where the typical values of  $\lambda$  could be 2, 4, or 8. The subscript  $l$  and  $h$  indicate *low-resolution* and *high-resolution*, respectively.

#### 3.1.3. WSI-level cancer prognosis

Only with WSI-level labels, DSCA needs to learn WSI-level representations from multiple dual-resolution patches for cancer prognosis prediction in a weakly-supervised manner. Similar to bag-level MIL, WSI-level representation learning also has two essential steps: patch embedding learning and global patch pooling (or aggregation).

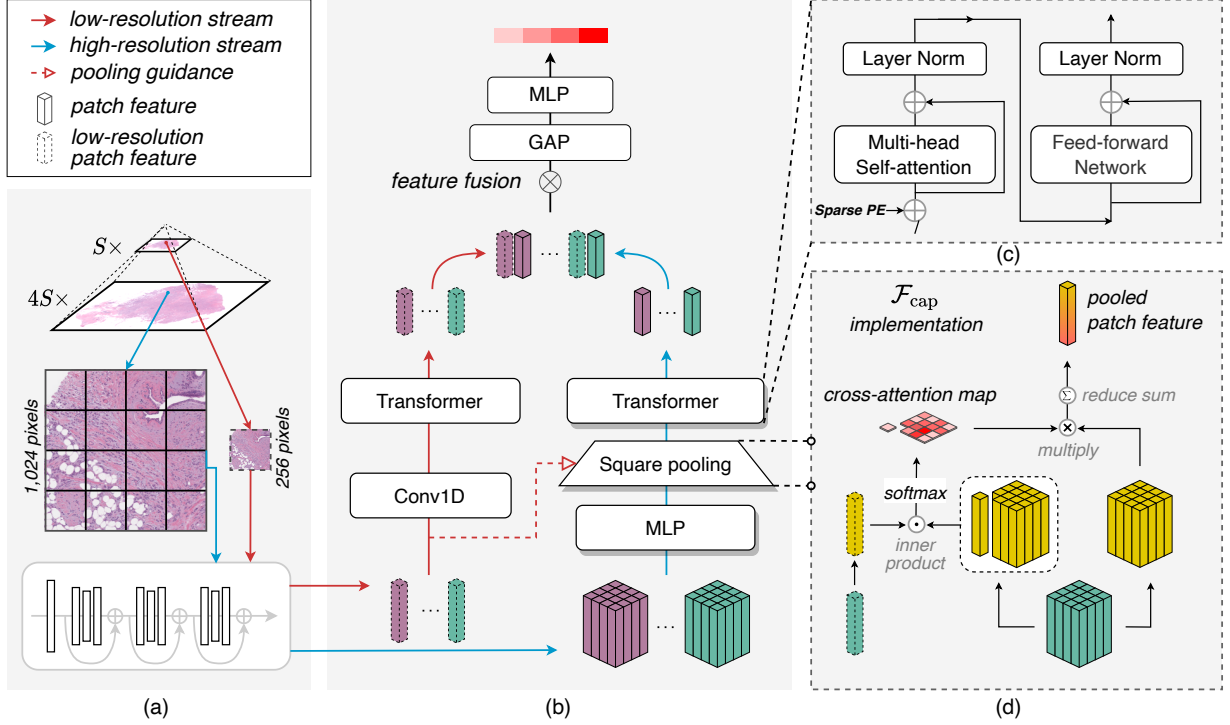


Figure 3: Overview of our DSCA scheme (best viewed in color). We illustrate our scheme using  $\lambda = 4$  and  $a = 256$ . (a) Spatially-aligned dual-resolution patching:  $S \times$  and  $4S \times$  images are sliced into non-overlapping patches and their features are extracted by a pre-trained model. (b) DSCA architecture. (c) Transformer encoder in DSCA. (d) Cross-attention pooling  $\mathcal{F}_{\text{cap}}$ : it’s an implementation of square pooling that pools high-resolution tokens under the guidance of low-resolution ones.

### 3.2. Spatially-aligned dual-resolution patching

First of all, we derive patches from the WSIs at two magnifications. The illustration of WSI pre-processing can be found in Figure 3(a). Specifically, for one WSI, we slice it at a low resolution ( $S \times$ ) and obtain the image patches with  $a \times a$  pixels ( $a$  is 256 usually). Then we slice the same WSI at a high resolution ( $\lambda S \times$ ), generating patches with  $a \times a$  pixels similarly. Moreover, as shown in Figure 3(a), a  $S \times$  patch is exactly spatially-aligned to the  $\lambda^2$  patches at  $\lambda S \times$  (*i.e.*, a square grid of  $\lambda \times \lambda$  cells). Lastly, we use a truncated ResNet-50 model (He et al., 2016) pre-trained on ImageNet (Deng et al., 2009) to extract instance features from each patch, following (Lu et al., 2021).

Given one patient with multiple WSIs, we denote its processed patch tokens at  $S \times$  and  $\lambda S \times$  by

$$\mathbf{X}_l \in \mathbb{R}^{m \times d} \text{ and } \mathbf{X}_h \in \mathbb{R}^{\lambda^2 m \times d},$$

respectively, where  $m$  is the number of  $S \times$  patches and  $d$  is the dimensionality of token. Comparing to  $\mathbf{X}_h$ ,  $\mathbf{X}_l$  contains coarser features and has a larger receptive field. Conversely,  $\mathbf{X}_h$  can provide more local and fine-grained information. This complementary nature helps to enhance the visual representation of gigapixel WSIs.

### 3.3. Dual-stream token embedding

#### 3.3.1. Low-resolution stream

For this stream, we adopt a one-dimensional convolution layer as its token embedding layer for simplicity.  $\mathbf{X}_l$  is padded

with zeros to keep the resolution. We write the output of this convolution layer by

$$\mathbf{E}_l = \text{Conv1D}(\mathbf{X}_l; k, s), \quad (3)$$

where  $\mathbf{E}_l \in \mathbb{R}^{m \times d_e}$  and  $d_e (< d)$  is the dimensionality of token embedding.  $k$  and  $s$  denote kernel size and stride length, respectively. Conv1D also plays a role of dimension reduction in token embedding. Moreover, 1D-convolution could integrate the individual patches within overlapping convolution windows, hence outputting overlapping token embeddings. This way could help to obtain more local continuity in tokens, as demonstrated in (Wang et al., 2021).

#### 3.3.2. High-resolution stream

In the high-resolution stream used for  $\lambda S \times$  patches, we take all the tokens in a  $\lambda \times \lambda$  square grid as a unit, and employ a token embedding operator for all these units. Specifically, we firstly reshape  $\mathbf{X}_h$  into square sequences, which is implemented by the function,  $\text{resize} : \mathbb{R}^{\lambda^2 m \times d} \rightarrow \mathbb{R}^{m \times \lambda \times \lambda \times d}$ . Then, the reshaped input goes through a token embedding layer and an activation layer in turn, written as

$$\mathbf{O}_h = \sigma(\rho(\text{resize}(\mathbf{X}_h))), \quad (4)$$

$$\rho : \mathbb{R}^{m \times \lambda \times \lambda \times d} \rightarrow \mathbb{R}^{m \times \lambda \times \lambda \times d_e},$$

where  $\sigma$  is an activation function and  $\mathbf{O}_h \in \mathbb{R}^{m \times \lambda \times \lambda \times d_e}$ . We utilize a simple implementation, MLP (multi-layer perceptron), for  $\rho$ . MLP calculates each token embedding individually,

thereby generating compact token embeddings without keeping local continuity. It is worth noting that, here we do not adopt a convolution-based implementation to produce overlapping embeddings, like that in the low-resolution stream. It is because, in the high-resolution stream, overlapping embedding may have greater potential to incur more information redundancy, as gigapixel WSIs have obviously-lower information density than natural images. We will further discuss this in experiments.

### 3.4. Square pooling with cross-attention

After high-resolution token embedding, we further apply a square pooling layer implemented by cross-attention to high-resolution tokens ( $\mathbf{O}_h$ ), for the two purposes: (i) significantly decreasing the number of high-resolution tokens and enabling the closely-followed Transformer to learn token dependency efficiently; (ii) handling the potential semantical gap between low- and high-resolution tokens via a cross-attention mechanism, so as to make the fusion of two resolution tokens smoother.

Specifically, our token pooling operator is similarly applied to square units, defined by  $\mathcal{F} : \mathbb{R}^{m \times \lambda \times \lambda \times d_e} \rightarrow \mathbb{R}^{m \times d_e}$ . As illustrated in Figure 3(d), we implement a cross-attention-based method for  $\mathcal{F}$ , written as  $\mathcal{F}_{\text{cap}}$ . In short,  $\mathcal{F}_{\text{cap}}$  uses the attention scores mapped from dual-stream tokens to perform a weighted pooling for high-resolution tokens. Namely, our square pooling with cross-attention is implemented by

$$\begin{aligned} \mathbf{Q}_l &= \mathbf{X}_l \mathbf{W}_l, \\ \mathbf{E}_h &= \mathcal{F}_{\text{cap}}(\mathbf{O}_h; \mathbf{Q}_l), \end{aligned} \quad (5)$$

where  $\mathbf{E}_h \in \mathbb{R}^{m \times d_e}$  and  $\mathbf{W}_l \in \mathbb{R}^{d \times d_e}$ .  $\mathbf{W}_l$  is a projection matrix to make the token dimension of  $\mathbf{Q}_l$  same to  $\mathbf{O}_h$ . Moreover, taking a low-resolution token (denoted as  $\mathbf{z}_l \in \mathbb{R}^{1 \times d_e}$ ) and its respective high-resolution tokens (denoted as  $\mathbf{z}_h \in \mathbb{R}^{\lambda^2 \times d_e}$ ) as examples,  $\mathcal{F}_{\text{cap}}$  can be written by

$$\mathcal{F}_{\text{cap}}(\mathbf{z}_h; \mathbf{z}_l) = \text{softmax}\left(\frac{\mathbf{z}_l \mathbf{W}_q (\mathbf{z}_h \mathbf{W}_k)^T}{\sqrt{d_e}}\right) \mathbf{z}_h \mathbf{W}_v, \quad (6)$$

where  $\mathbf{W}_q, \mathbf{W}_k, \mathbf{W}_v \in \mathbb{R}^{d_e \times d_e}$  are the projection matrices for query, key, and value, respectively.

Our cross-attention scheme does spatial attention pooling for large region ( $\lambda a \times \lambda a$  pixels). It enables high-resolution tokens with local and fine-grained features to pool under the guidance of a token with a global view. Therefore, the result of cross-attention pooling is expected to selectively preserve certain fine-grained information based on the spatial response of high-resolution patches to their global view. In addition, with the square pooling, the number of high-resolution tokens can be decreased by a factor of  $\frac{1}{\lambda^2}$ , becoming identical to the number of low-resolution ones.

## 3.5. Transformer-based token dependency learning

### 3.5.1. Sparse positional embedding

We calculate the positional embedding (PE) of tokens similar to Transformer (Vaswani et al., 2017), rather than ViT (Dosovitskiy et al., 2021), because, unlike general cases, the size of

tokens (*i.e.*, the value of  $m$ ) varies across WSIs. In addition, there is a problem of spatially-sparse distribution in tokens, as we filter the patches without any tissue region in WSI patching.

To solve this, we put all WSIs from one patient in a row and then map the coordinates of all available patches to a discrete domain without breaking their relative locations. In this way, we can encode the position information of tokens while preserving intrinsic spatially-sparse property, even for multiple WSIs. For simplicity, we write the result of sparse PE as

$$\mathbf{PE} \in \mathbb{R}^{m \times d_e}.$$

### 3.5.2. Dependency learning

As shown in Figure 3(c), we employ a Transformer encoder at the end of either stream to learn potential token dependencies, as Transformer has shown great success in capturing token dependencies (Vaswani et al., 2017). This encoder is a vanilla Transformer encoder that consists of a multi-head self-attention layer and a feed-forward network. We denote these two parts by  $\text{MSA} : \mathbb{R}^{m \times d_e} \rightarrow \mathbb{R}^{m \times d_e}$  and  $\text{FFN} : \mathbb{R}^{m \times d_e} \rightarrow \mathbb{R}^{m \times d_e}$ , respectively. The Transformer encoder,  $\mathcal{T} : \mathbb{R}^{m \times d_e} \rightarrow \mathbb{R}^{m \times d_e}$ , can be expressed by

$$\begin{aligned} \mathcal{T} &= \zeta \circ \varphi, \\ \zeta(x) &= \text{LN}(\text{MSA}(x) + x), \\ \varphi(x) &= \text{LN}(\text{FFN}(x) + x), \end{aligned} \quad (7)$$

where LN is a layer normalization function (Ba et al., 2016). Based on Equation 7, we can get the outputs as follows:

$$\mathbf{V}_l = \mathcal{T}_l(\mathbf{E}_l + \mathbf{PE}) \text{ and } \mathbf{V}_h = \mathcal{T}_h(\mathbf{E}_h + \mathbf{PE}).$$

## 3.6. Dual-stream feature fusion

Stream feature fusion (FF) is implemented by the following function:

$$\mathbf{F} = \text{FF}(\{\mathbf{V}_l, \mathbf{V}_h\}). \quad (8)$$

We use a simple implementation for FF, feature concatenating, defined by

$$\text{cat} : \mathbb{R}^{2m \times d_e} \rightarrow \mathbb{R}^{m \times 2d_e}.$$

In addition, we consider an adding version for FF. Their results are shown in experiments.

## 3.7. Prognosis prediction

### 3.7.1. Output layer

We utilize a global attention pooling (GAP) (Ilse et al., 2018) to obtain WSI-level features. Specifically, all available tokens are weighted by their respective attention scores, and then they are aggregated into a global vector. This global vector is finally employed to infer prognosis prediction via a multi-layer perceptron (MLP). Thus, our output layer implements

$$\begin{aligned} \mathbf{H} &= \text{GAP}(\mathbf{F}), \\ \mathbf{O} &= \text{sigmoid}(\text{MLP}(\mathbf{H})), \end{aligned} \quad (9)$$

where  $\text{GAP} : \mathbb{R}^{m \times d_o} \rightarrow \mathbb{R}^{d_o}$ ,  $\text{MLP} : \mathbb{R}^{d_o} \rightarrow \mathbb{R}^{n_t}$ , and  $\mathbf{O} \in \mathbb{R}^{n_t}$  is the prediction of individual hazard function.  $d_o$  is the dimensionality of WSI-level features, which equals  $2d_e$ .  $n_t$  denotes the number of time points considered in survival prediction.

Table 2: Statistic of datasets. The number of patches is measured after slicing WSIs at 20× magnification.

Name	NLST	TCGA	
		BRCA	LGG
primary site	lung	breast	brain
storage size	0.76 TB	0.98 TB	0.88 TB
death ratio	35.9%	13.5%	23.4%
# patients	447	978	486
# WSIs	1,222	1,043	836
# patches (20×)	3,955,344	3,228,480	2,637,456
$\frac{\# \text{ patches}}{\# \text{ WSIs}} (20\times)$	3,236.8	3,095.4	3,154.9

### 3.7.2. Loss function

The loss function for optimizing our DSCA network is a negative log-likelihood function (Zadeh & Schmid, 2021) used for training discrete deep survival models:

$$L = L_{\text{uncensored}} + (1 - \alpha)L_{\text{censored}},$$

$$L_{\text{uncensored}} = - \sum_{(\mathcal{P}_i, t_i, c_i) \in T} \left\{ (1 - c_i) \cdot \log(S(t_i - 1) \cdot h(t_i)) \right\}, \quad (10)$$

$$L_{\text{censored}} = - \sum_{(\mathcal{P}_i, t_i, c_i) \in T} \left\{ c_i \cdot \log(S(t_i)) \right\},$$

where  $\alpha \in \mathbb{R}_0^+$ ,  $h(t_i)$  is the  $t_i$ -th element of the network prediction  $\mathbf{O}$ , and  $S(t_i) = \prod_{s=1}^{t_i} (1 - h(s))$ . In survival analysis,  $h(t)$  is a hazard function, and  $S(t)$  is a survival function indicating the probability of surviving time  $t$ . This survival function does not rely on any assumption about the form of hazard function. By contrast, the popular loss functions (Cox, 1975; Liu et al., 2021), based on Cox model, have a strong assumption—proportional hazard. We thereby adopt Equation 10 to optimize DSCA, as suggested in (Zadeh & Schmid, 2021).

## 4. Experiments and results

### 4.1. Datasets

We validate our DSCA on the three large publicly-available datasets: National Lung Screening Trial (NLST) (Team, 2011), BRCA Cancer (BRCA), and Low-Grade Glioma (LGG). The last two datasets are from The Cancer Genome Atlas (Kandath et al., 2013). As shown in Table 2, we obtain a total of 3,101 WSIs from 1,911 patients, after excluding unavailable WSIs and the patients with unknown follow-up status. Note that there is not any other form of data curation except that we mentioned.

From Table 2, we can see that the overall death ratio of breast cancer is apparently smaller than that of the other two cancer diseases. The prognosis event of interest that we predict is the overall survival (OS), a typical endpoint in survival analysis. We can notice that there are usually more than 3,000 patches per WSI at 20× on average.

### 4.2. Experimental setup

#### 4.2.1. Evaluation metrics

We adopt Concordance Index (C-Index) (Heagerty & Zheng, 2005) to measure model performance. C-Index is a widely-used

evaluation metric in survival analysis, which mainly assesses the model ability of survival risk discrimination. It is written as

$$\text{C-Index} = \frac{1}{M} \sum_{i: c_i=0} \sum_{j: t_i < t_j} I(\hat{y}_i > \hat{y}_j) \in [0, 1],$$

where  $I(\cdot)$  is an indicator function and  $M$  is the number of all comparable pairs. We compute  $\hat{y}$  by a negative average over the survival probabilities at all time points, *i.e.*,  $\hat{y} = \frac{1}{n_i} \sum_{k=1}^{n_i} S(k)$ . The C-Index would be larger if a model could predict higher risks for the patients who die earlier.

#### 4.2.2. Model evaluation

We use 5-fold cross-validation to evaluate all the models in our experiments. In each fold training, we retain the 20% training set as a validation set for early stopping and learning rate adjusting. Data splitting is ensured to conduct at patient-level. To assess the computation efficiency of models in space and time complexity (Tan et al., 2020), we report the size of trainable parameters (Model Size) and the theoretical amount of Multiply-Accumulate operations (# MACs) in models, respectively, by using a package *ptflops*<sup>1</sup>.

#### 4.2.3. Dual-resolution setup

We adopt 20× for high resolution in our experiments, because this resolution is a common choice in previous literature, *e.g.*, Li et al. (2018); Di et al. (2020); Chen et al. (2021); Shao et al. (2021a); Huang et al. (2021); Li et al. (2021b); Shao et al. (2021b); Li et al. (2021a); Zhang et al. (2022); Chen et al. (2022). Moreover, this resolution could capture cell-tissue interactions for downstream prediction, and its computational cost is reasonable. In addition, we select 5× for low resolution, *i.e.*,  $\lambda = 4$ , as this resolution could present tissue phenotype, contributing to prognosis prediction (Chen et al., 2022), as shown in Figure 1.

#### 4.2.4. Implementation details

For WSI patching, we set the size of patch to  $256 \times 256$  pixels, *i.e.*,  $a = 256$ , following Lu et al. (2021). And  $d = 1024$ , output by a truncated ResNet-50 model. In Conv1D, we empirically set  $k = 5$  and  $s = 3$ . For each dataset we use the same settings: 150 epochs, a learning rate of  $8 \times 10^{-5}$ , a gradient accumulation step of 16, an optimizer of Adam with a weight decay rate of  $5 \times 10^{-4}$ , and a loss function given by Equation 10. Learning rate decays by a factor of 0.5 if a validation loss does not decrease in the past 10 epochs. Model training stops if a validation loss does not decrease in the past 30 epochs. For other hyper-parameters, we empirically set  $d_e$  to 384 and  $n_t$  to 4. All experiments run on a machine with  $2 \times \text{V100s}$  (32G) GPUs.

#### 4.2.5. Baseline comparisons

Deep Sets (Zaheer et al., 2017) and Attention-MIL (Ilse et al., 2018) are adopted as baselines since they are classical MIL approaches. And the approaches presented in Table 1 are also

<sup>1</sup><https://pympi.org/project/ptflops>

Table 3: Prognosis prediction performance measured by 5-fold cross-validation. The asterisk (\*) indicates that the method was originally proposed for WSI classification. Baseline comparisons are elaborated in Section 4.2.5. The # MACs of model are measured using a bag with 210 patches at low resolution and 3,360 patches at high resolution. We use the same patch feature extractor and loss function in all methods for fair comparisons.

Method	Mean C-Index (Standard Deviation)			Model Size	# MACs
	NLST	BRCA	LGG		
Deep Sets (Zaheer et al., 2017)	0.47271 (0.08325)	0.47106 (0.03884)	0.60080 (0.07250)	657.16K	1.76G
Attention-MIL (Ilse et al., 2018)	0.57157 (0.09022)	0.54118 (0.06273)	0.60820 (0.04624)	920.07K	2.64G
DeepAttnMISL (Yao et al., 2020)	0.55062 (0.06372)	0.53234 (0.03403)	0.61963 (0.05941)	1.18M	1.77G
DeepGraphConv (Li et al., 2018)	0.57931 (0.06061)	0.54254 (0.07946)	0.61954 (0.07918)	790.02K	2.42G
Patch-GCN (Chen et al., 2021)	0.58588 (0.08245)	0.49325 (0.02457)	0.67261 (0.01605)	1.38M	3.75G
SeTranSurv (Huang et al., 2021)	0.54203 (0.10244)	0.55339 (0.09756)	0.59912 (0.03948)	1.58M	1.22G
TransMIL* (Shao et al., 2021b)	0.59535 (0.03053)	0.53175 (0.06944)	0.69049 (0.05121)	2.67M	9.55G
H <sup>2</sup> MIL* (Hou et al., 2022)	0.60129 (0.03948)	0.53125 (0.05582)	0.56867 (0.11425)	860.18K	4.94G
<b>DSCA (ours)</b>	<b>0.66803</b> (0.05817)	<b>0.61224</b> (0.05350)	<b>0.70181</b> (0.04321)	6.31M	2.51G

used for comparisons, *except* (i) BDOCOX (Shao et al., 2021a) and RankSurv (Di et al., 2020): source codes are unavailable; (ii) DSMIL (Li et al., 2021b) and DTFD-MIL (Zhang et al., 2022): inapplicable to survival prediction tasks (refer to Section 2.3). Moreover, WSISA (Zhu et al., 2017) and DT-MIL (Li et al., 2021b) are not among our baselines, because the former is not a MIL model and the latter cannot be used for spatially-sparse patches. HIPT (Chen et al., 2022) is based on a pre-training strategy so it is also not used. Despite unavailable source codes, SeTranSurv (Huang et al., 2021) is also in our baselines, since it is the first Transformer-based prognosis model. An inhouse-implementation is used for it.

### 4.3. Prognosis prediction

#### 4.3.1. Overall performance

The results of model performance are shown in Table 3. From this table, we can summarize that (i) our DSCA scheme achieves the best performances in C-Index on three datasets, and it shows obvious advantages on NLST and BRCA; (ii) our DSCA model generally has more learnable parameters but fewer computational costs. Furthermore, from Table 3 we have the following empirical analysis.

(1) We can notice that the classification-oriented model, TransMIL, is competitive with existing models. Because TransMIL specially devises a convolution-based positional encoding module to extract discriminative global features, as described in (Shao et al., 2021b). However, this module usually brings huge computational costs (9.55G MACs, see Table 3). By contrast, our DSCA has an obviously-lower computational cost (2.51G MACs), owing to the square pooling layer which largely decreases the number of high-resolution patches while exploiting fine-grained features. Moreover, our scheme achieves better performance than TransMIL, especially on NLST and BRCA. In addition, it is observed that our DSCA network has more model parameters (6.31M) than TransMIL (2.67M), which indicates that our model has a higher space complexity (or memory consumption). This is largely due to the low-resolution stream of DSCA. Please refer to our ablation study for more details.

(2) As a multi-resolution scheme similar to our DSCA, the classification-oriented H<sup>2</sup>MIL performs not well in cancer prognosis. A possible reason is that H<sup>2</sup>MIL has too few learnable model parameters (860.18K) to handle a more complex task, cancer prognosis. Besides that, we can notice that, although H<sup>2</sup>MIL has few model parameters, its dense cross-resolution graph edges (see Figure 2(b)) incur a high computation load (4.94G). Instead of explicitly using cross-resolution connections like H<sup>2</sup>MIL, our DSCA adopts cross-attention to deal with the potential semantical gap between dual-resolution patches. We will dive into the core of DSCA through ablation studies.

(3) Our DSCA gains a C-Index improvement of 6.7%, 5.9%, and 1.1% on NLST, BRCA, and LGG, respectively, in comparison with SOTA baselines. This empirical result demonstrates that the proposed DSCA could often outperform existing mainstream approaches in WSI cancer prognosis.

#### 4.3.2. Risk stratification

We also assess the model’s ability in risk stratification, which is also a widely-used evaluation for survival analysis models. Specifically, we first aggregate out-of-sample risk predictions from the validation folds of a single dataset, and then stratify patients into two risk groups. Patients belong to a high-risk group if their risk predictions are higher than the median; otherwise, a low-risk one. Finally, we utilize the ground truth of patient survival time to plot the survival distributions of two risk groups, as shown in the Kaplan-Meier survival curves of Figure 4, and use a logrank test to measure if the difference of two survival distributions is statistically significant (P-Value < 0.05). A survival model is of good risk discrimination if there is a significant difference between high- and low-risk groups.

From Figure 4, we can see that our models, trained on three cancer types separately, can always classify patients into a high- or low-risk group with significant differences (P-Value<0.01). It means that our models could accurately identify poor or good prognoses from the WSIs of cancer patients. Moreover, the stratification differences given by our method are clearer than that given by others on NLST and BRCA, seen from P-Values.

Table 4: Ablation study on DSCA. Results are assessed by 5-fold cross-validation. Res. refers to Resolution.

Dual-stream		Cross-attention	Mean C-Index			Model Size	# MACs
Low Res.	High Res.		NLST	BRCA	LGG		
✓	-	-	0.66174	0.60193	0.57553	3.15M	695.39M
-	✓	-	0.65914 <sub>-0.00260</sub>	0.60820 <sub>+0.00627</sub>	0.65614 <sub>+0.08061</sub>	1.58M	1.61G
✓	✓	-	0.66887 <sub>+0.00973</sub>	0.59599 <sub>-0.01221</sub>	0.68965 <sub>+0.03351</sub>	5.32M	2.43G
✓	✓	✓	0.66803 <sub>-0.00084</sub>	0.61224 <sub>+0.01625</sub>	0.70181 <sub>+0.01216</sub>	6.31M	2.51G

Table 5: Comparison of the different token embedding layers in the high-resolution stream.

$\rho$	Mean C-Index			Model Size	# MACs
	NLST	BRCA	LGG		
MLP	0.66803	0.61224	0.70181	6.31M	2.51G
Conv2D	0.66981 <sub>+0.00178</sub>	0.58552 <sub>-0.02672</sub>	0.67344 <sub>-0.02837</sub>	9.45M	13.08G

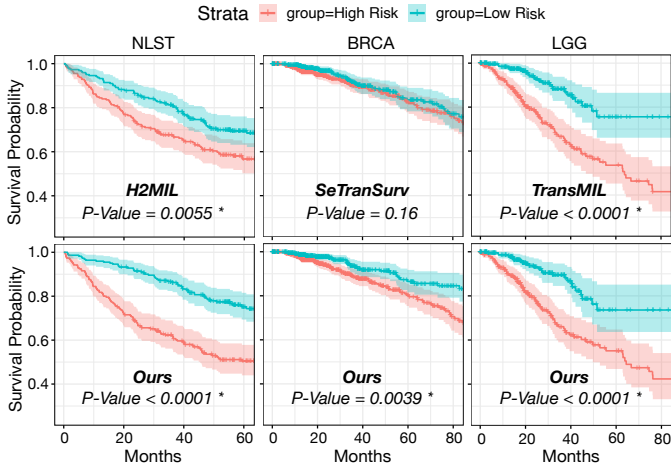


Figure 4: Risk stratification. Our method and the other best ones (in C-Index) are shown. The Kaplan-Meier survival curves are plotted using ground-truth labels. The P-Value is computed by a logrank test to measure the significance of survival differences between two risk groups.

#### 4.4. Ablation study

##### 4.4.1. Dual-stream and cross-attention

To study how the key components, dual-stream and cross-attention, affect DSCA’s performance, we start from a single-stream version that only processes single-resolution patches (*i.e.*, in which one sub-stream is removed from DSCA). Note that, for the DSCA only with a high-resolution stream, we use a simple function, mean-pooling, to implement its square pooling layer. Then, we improve single-stream networks by completing dual-stream and further replacing mean-pooling with our cross-attention pooling. The results are shown in Table 4.

From Table 4, we can observe the following empirical facts.

(i) Comparing the high-resolution stream with a low-resolution one, the C-Index on LGG has a clear rise ( $\sim 0.08$ ), and the C-Index on NLST and BRCA have no obvious changes (the highest is  $\sim 0.006$ ). (ii) Transforming high-resolution stream into dual-stream, the C-Index on both LGG and NLST have improvements, and the improvement on LGG is more apparent ( $\sim 0.03$ ); whereas the C-Index on BRCA drops by  $\sim 0.01$  (this

drop is fixed afterward by adding cross-attention). (iii) After applying cross-attention pooling, C-Index performance can be further boosted, except for a slight drop ( $< 0.001$ ) on NLST. (iv) Moreover, from Table 4, we can see that the model size of DSCA is greatly increased (from 1.58M to 6.31M) compared to the beginning version. This is largely due to the involvement of Conv1D. Despite the increase of model size in DSCA, we notice that the amount of MACs remains relatively small (1.61G–2.51G), owing to our square pooling layer, especially for enormous high-resolution patches.

Finally, by combining these two vital components, our DSCA could often achieve the best performances on three datasets. This ablation study suggests that our key idea, dual-stream with cross-attention, indeed contributes to DSCA.

##### 4.4.2. High-resolution token embedding

We compare the two different implementations of the high-resolution token embedding layer ( $\rho$ ), *i.e.*, MLP and Conv2D, as discussed in Section 3.3.2. Comparison results are shown in Table 5. From these results, we can summarize that the high-resolution token embedding implemented by Conv2D cannot always bring apparent positive effects on model performance, as it only has an ignorable improvement ( $< 0.002$ ) on NLST; instead, it largely increases the model size by 3.14M and the # MACs by 10.57G, in comparison with MLP.

These facts indicate that the way of overlapping embedding in Conv2D may not be suitable for high-resolution WSI patches though it has been demonstrated to be effective for natural images (Wang et al., 2021). By contrast, the way of compact token embedding in MLP is almost always shown to be better in both model performance and computation efficiency, which exactly demonstrates our argument (see Section 3.3.2).

##### 4.4.3. Network hyper-parameters

We test the effect of important network hyper-parameters on model performance and show its results as follows.

(1) Sparse positional embedding (PE). The details of sparse PE can be found in Section 3.5.1. We examine the DSCA network with or without sparse PE, and show their results in Table

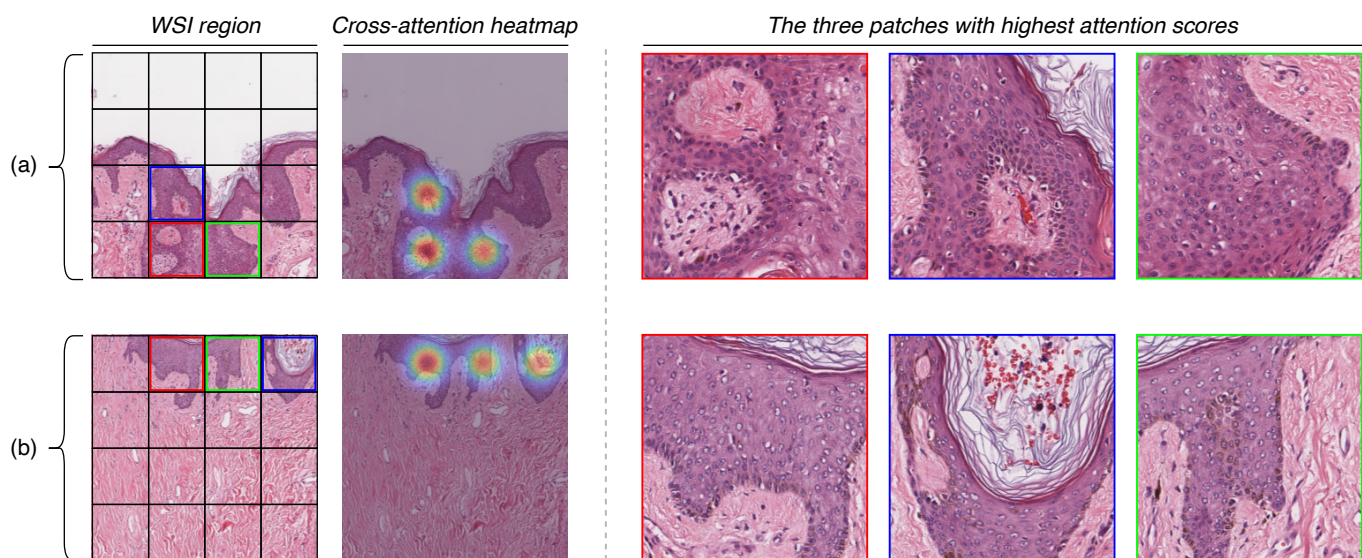


Figure 5: Visualization of cross-attention maps on the region (a) and (b). Patches are exhibited in descending order according to their attention scores. Each patch region (left) is at 5× magnification and with  $256 \times 256$  pixels. All the three selected patches are at 20× magnification and with the same scale.

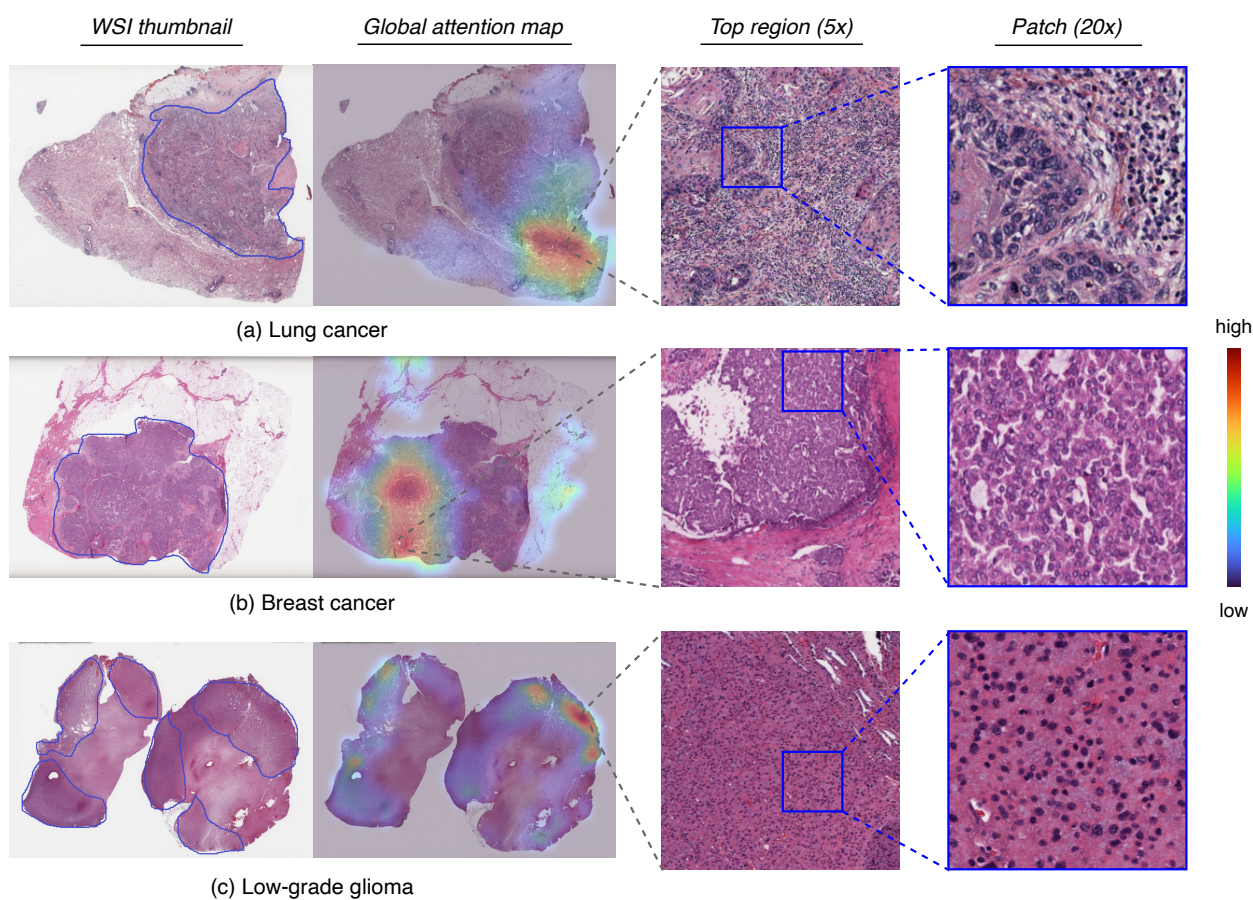


Figure 6: Visualization of global attention maps on the three WSIs with different cancer diseases. The blue lines in WSI thumbnails are the annotations of the tumorous region of interest. The 50% of regions with lower attention are assigned with zero scores for a better view. Top region means the region with high attention.

6. From this table, we can find that the network with sparse PE achieves better performances on both NLST and BRCA; on LGG, the network without sparse PE is better.

Table 6: Effect of sparse positional embedding (PE) on DSCA.

Sparse PE	Mean C-Index		
	NLST	BRCA	LGG
✓	0.66803	0.61224	0.68740
✗	0.65901	0.59148	0.70181

(2) Stream feature fusion (FF). We also examine different implementations for the feature fusion of dual-stream tokens, concatenating and adding. From the results shown in Table 7, we see that only on NLST, the way of adding leads that of concatenating by a quite narrow margin ( $\sim 0.004$ ). Thus we set the way of stream FF to concatenating for all experiments.

Table 7: Effect of different feature fusion (FF) implementations on DSCA.

Stream FF	Mean C-Index		
	NLST	BRCA	LGG
concatenating	0.66803	0.61224	0.70181
adding	0.67216	0.61115	0.68121

#### 4.5. Interpretability and visualization

To intuitively understand the effect of cross-attention pooling, we randomly select two regions from breast cancer tissues and visualize their cross-attention results. Specifically, at first, we obtain cross-attention scores (averaged over multiple attention heads) from each  $5\times$  region and its respective  $20\times$  patches (presented as a  $4\times 4$  square grid), by Equation 6. Then, we select the three patches with the highest attention scores, and show their fine-grained cellular details. As shown in Figure 5, we can observe that the cross-attention guided by global views could enable the model to focus on informative patches, *e.g.*, the patches with normal or tumorous cells. Moreover, almost all the top attention patches contain many irregular cells. These cells are highly-different in size and shape (see Figure 5), often indicating a poor cancer prognosis (Alizadeh et al., 2015). These visualization results show that, discriminative fine-grained features could be distilled from high-resolution patches via cross-attention pooling, thus facilitating a more accurate prognosis prediction.

In addition, we further show the result of global attention pooling (see Section 3.7.1, output layer), to observe which region has a high correlation with cancer prognosis. As shown in Figure 6, our model could capture local regions for prognosis prediction, and those predicted high-correlation regions tend to appear in RoI (region of interest) annotations. Moreover, we could see some highly-differentiated and irregular cells in these regions ( $5\times$ ) and their enlarged patch images ( $20\times$ ). Especially for the sample with lung cancer, there are clear differences in cell morphology between the cells located on the left side and the right side, as shown in the leftmost  $20\times$  patch in Figure

6(a). These observations suggest that our model could capture discriminative regions and enjoy good interpretability for cancer prognosis.

## 5. Conclusion

This paper proposed a dual-stream network with cross-attention (DSCA) to fully utilize WSI pyramids for cancer prognosis. Unlike existing multi-resolution schemes for WSIs, we devised two sub-streams to process the patches with two resolutions. Moreover, we proposed a square pooling layer implemented by cross-attention to efficiently learn fine-grained features and make the fusion of dual-stream features smoother. A total of 3,101 WSIs from 1,911 patients is used to validate our scheme and compare our scheme with state-of-the-art approaches. Our experimental results show that: i) the key idea of dual-stream and cross-attention indeed contributes to DSCA’s performance, ii) our DSCA network is more efficient than a typical multi-resolution network ( $H^2MIL$ ), and iii) the proposed DSCA could outperform existing state-of-the-art methods in cancer prognosis by an average C-Index improvement of around 4.6%. We hope that the proposed DSCA could encourage more works to explore WSI pyramids for broad downstream tasks, and our dual-stream architecture could serve as an effective tool for WSI-based cancer prognosis.

In the future, we will explore other efficient strategies of multi-scale feature fusion for gigapixel WSIs, such as a reverse or bi-directional fusion of multi-resolution features. Moreover, we will study how to exploit feature pyramids directly and efficiently in WSIs, similar to the way of modern ConvNets for natural images. In the light of the development of computer vision, we believe that WSI pyramid hierarchy would become a promising research topic in computational pathology.

## References

- Adelson, E. H., Anderson, C. H., Bergen, J. R., Burt, P. J., & Ogden, J. M. (1984). Pyramid methods in image processing. *RCA engineer*, 29, 33–41.
- Alizadeh, A. A., Aranda, V., Bardelli, A., Blanpain, C., Bock, C., Borowski, C., Caldas, C., Califano, A., Doherty, M., Elsner, M. et al. (2015). Toward understanding and exploiting tumor heterogeneity. *Nature medicine*, 21, 846–853.
- Ba, J. L., Kiros, J. R., & Hinton, G. E. (2016). Layer normalization. *arXiv preprint arXiv:1607.06450*, .
- Bankhead, P., Loughrey, M. B., Fernández, J. A., Dombrowski, Y., McArt, D. G., Dunne, P. D., McQuaid, S., Gray, R. T., Murray, L. J., Coleman, H. G. et al. (2017). Qupath: Open source software for digital pathology image analysis. *Scientific reports*, 7, 1–7.
- Bremnes, R. M., Dønnem, T., Al-Saad, S., Al-Shibli, K., Andersen, S., Sirera, R., Camps, C., Martinez, I., & Busund, L.-T. (2011). The role of tumor stroma in cancer progression and prognosis: Emphasis on carcinoma-associated fibroblasts and non-small cell lung cancer. *Journal of Thoracic Oncology*, 6, 209–217. doi:<https://doi.org/10.1097/JTO.0b013e3181f8a1bd>.
- Carbonneau, M.-A., Cheplygina, V., Granger, E., & Gagnon, G. (2018). Multi-instance learning: A survey of problem characteristics and applications. *Pattern Recognition*, 77, 329–353.
- Chen, R. J., Chen, C., Li, Y., Chen, T. Y., Trister, A. D., Krishnan, R. G., & Mahmood, F. (2022). Scaling vision transformers to gigapixel images via hierarchical self-supervised learning. In *Proceedings of the IEEE/CVF Conference on Computer Vision and Pattern Recognition* (pp. 16144–16155).

- Chen, R. J., Lu, M. Y., Shaban, M., Chen, C., Chen, T. Y., Williamson, D. F., & Mahmood, F. (2021). Whole slide images are 2d point clouds: Context-aware survival prediction using patch-based graph convolutional networks. In *International Conference on Medical Image Computing and Computer-Assisted Intervention* (pp. 339–349). Springer.
- Cox, D. R. (1975). Partial likelihood. *Biometrika*, *62*, 269–276.
- De Boer, A. G., Taskila, T., Ojajarvi, A., Van Dijk, F. J., & Verbeek, J. H. (2009). Cancer survivors and unemployment: a meta-analysis and meta-regression. *JAMA*, *301*, 753–762.
- Deng, J., Dong, W., Socher, R., Li, L.-J., Li, K., & Fei-Fei, L. (2009). Imagenet: A large-scale hierarchical image database. In *2009 IEEE conference on computer vision and pattern recognition* (pp. 248–255). IEEE.
- Di, D., Li, S., Zhang, J., & Gao, Y. (2020). Ranking-based survival prediction on histopathological whole-slide images. In *International Conference on Medical Image Computing and Computer-Assisted Intervention* (pp. 428–438). Springer.
- Dietterich, T. G., Lathrop, R. H., & Lozano-Pérez, T. (1997). Solving the multiple instance problem with axis-parallel rectangles. *Artificial intelligence*, *89*, 31–71.
- Ding, S., Gao, Z., Wang, J., Lu, M., & Shi, J. (2022). Fractal graph convolutional network with mlp-mixer based multi-path feature fusion for classification of histopathological images. *Expert Systems with Applications*, (p. 118793).
- Dosovitskiy, A., Beyer, L., Kolesnikov, A., Weissenborn, D., Zhai, X., Unterthiner, T., Dehghani, M., Minderer, M., Heigold, G., Gelly, S., Uszkoreit, J., & Houlsby, N. (2021). An image is worth 16x16 words: Transformers for image recognition at scale. In *International Conference on Learning Representations*. URL: <https://openreview.net/forum?id=YicbFdNTTy>.
- Fu, B., Liu, P., Lin, J., Deng, L., Hu, K., & Zheng, H. (2019). Predicting invasive disease-free survival for early stage breast cancer patients using follow-up clinical data. *IEEE Transactions on Biomedical Engineering*, *66*, 2053–2064. doi:10.1109/TBME.2018.2882867.
- He, K., Zhang, X., Ren, S., & Sun, J. (2016). Deep residual learning for image recognition. In *Proceedings of the IEEE conference on computer vision and pattern recognition* (pp. 770–778).
- Heagerty, P. J., & Zheng, Y. (2005). Survival model predictive accuracy and roc curves. *Biometrics*, *61*, 92–105. doi:<https://doi.org/10.1111/j.0006-341X.2005.030814.x>.
- Hou, W., Yu, L., Lin, C., Huang, H., Yu, R., Qin, J., & Wang, L. (2022). H2-mil: Exploring hierarchical representation with heterogeneous multiple instance learning for whole slide image analysis. *Proceedings of the AAAI Conference on Artificial Intelligence*, *36*, 933–941. URL: <https://ojs.aaai.org/index.php/AAAI/article/view/19976>. doi:10.1609/aaai.v36i1.19976.
- Houssein, E. H., Emam, M. M., Ali, A. A., & Suganthan, P. N. (2021). Deep and machine learning techniques for medical imaging-based breast cancer: A comprehensive review. *Expert Systems with Applications*, *167*, 114161.
- Huang, Z., Chai, H., Wang, R., Wang, H., Yang, Y., & Wu, H. (2021). Integration of patch features through self-supervised learning and transformer for survival analysis on whole slide images. In *International Conference on Medical Image Computing and Computer-Assisted Intervention* (pp. 561–570). Springer.
- Ilse, M., Tomczak, J., & Welling, M. (2018). Attention-based deep multiple instance learning. In *International conference on machine learning* (pp. 2127–2136). PMLR.
- Kandath, C., McLellan, M. D., Vandin, F., Ye, K., Niu, B., Lu, C., Xie, M., Zhang, Q., McMichael, J. F., Wyczalkowski, M. A., Leiserson, M. D. M., Miller, C. A., Welch, J. S., Walter, M. J., Wendl, M. C., Ley, T. J., Wilson, R. K., Raphael, B. J., & Ding, L. (2013). Mutational landscape and significance across 12 major cancer types. *Nature*, *502*, 333–339.
- Li, B., Li, Y., & Eliceiri, K. W. (2021a). Dual-stream multiple instance learning network for whole slide image classification with self-supervised contrastive learning. In *Proceedings of the IEEE/CVF Conference on Computer Vision and Pattern Recognition* (pp. 14318–14328).
- Li, H., Yang, F., Zhao, Y., Xing, X., Zhang, J., Gao, M., Huang, J., Wang, L., & Yao, J. (2021b). Dt-mil: Deformable transformer for multi-instance learning on histopathological image. In *International Conference on Medical Image Computing and Computer-Assisted Intervention* (pp. 206–216). Springer.
- Li, R., Yao, J., Zhu, X., Li, Y., & Huang, J. (2018). Graph cnn for survival analysis on whole slide pathological images. In *International Conference on Medical Image Computing and Computer-Assisted Intervention* (pp. 174–182). Springer.
- Lin, T.-Y., Dollár, P., Girshick, R., He, K., Hariharan, B., & Belongie, S. (2017). Feature pyramid networks for object detection. In *Proceedings of the IEEE conference on computer vision and pattern recognition* (pp. 2117–2125).
- Liu, P., Fu, B., Yang, S. X., Deng, L., Zhong, X., & Zheng, H. (2021). Optimizing survival analysis of xgboost for ties to predict disease progression of breast cancer. *IEEE Transactions on Biomedical Engineering*, *68*, 148–160. doi:10.1109/TBME.2020.2993278.
- Liu, T., Su, R., Sun, C., Li, X., & Wei, L. (2022). Eocsa: Predicting prognosis of epithelial ovarian cancer with whole slide histopathological images. *Expert Systems with Applications*, *206*, 117643. doi:<https://doi.org/10.1016/j.eswa.2022.117643>.
- Lu, M. Y., Williamson, D. F., Chen, T. Y., Chen, R. J., Barbieri, M., & Mahmood, F. (2021). Data-efficient and weakly supervised computational pathology on whole-slide images. *Nature biomedical engineering*, *5*, 555–570.
- Moitra, D., & Mandal, R. K. (2020). Classification of non-small cell lung cancer using one-dimensional convolutional neural network. *Expert Systems with Applications*, *159*, 113564.
- Pati, P., Jaume, G., Fernandes, L. A., Foncubierta-Rodríguez, A., Feroce, F., Anniciello, A. M., Scognamiglio, G., Brancati, N., Riccio, D., Bonito, M. D. et al. (2020). Hact-net: A hierarchical cell-to-tissue graph neural network for histopathological image classification. In *Uncertainty for Safe Utilization of Machine Learning in Medical Imaging, and Graphs in Biomedical Image Analysis* (pp. 208–219). Springer.
- Pati, P., Jaume, G., Foncubierta-Rodríguez, A., Feroce, F., Anniciello, A. M., Scognamiglio, G., Brancati, N., Fiche, M., Dubruc, E., Riccio, D. et al. (2022). Hierarchical graph representations in digital pathology. *Medical image analysis*, *75*, 102264.
- Shao, W., Han, Z., Cheng, J., Cheng, L., Wang, T., Sun, L., Lu, Z., Zhang, J., Zhang, D., & Huang, K. (2019). Integrative analysis of pathological images and multi-dimensional genomic data for early-stage cancer prognosis. *IEEE transactions on medical imaging*, *39*, 99–110.
- Shao, W., Wang, T., Huang, Z., Han, Z., Zhang, J., & Huang, K. (2021a). Weakly supervised deep ordinal cox model for survival prediction from whole-slide pathological images. *IEEE Transactions on Medical Imaging*, *40*, 3739–3747.
- Shao, Z., Bian, H., Chen, Y., Wang, Y., Zhang, J., Ji, X., & Zhang, Y. (2021b). TransMIL: Transformer based correlated multiple instance learning for whole slide image classification. In A. Beygelzimer, Y. Dauphin, P. Liang, & J. W. Vaughan (Eds.), *Advances in Neural Information Processing Systems*. URL: <https://openreview.net/forum?id=LKUfuWxajHc>.
- Simonyan, K., & Zisserman, A. (2014). Very deep convolutional networks for large-scale image recognition. *arXiv preprint arXiv:1409.1556*.
- Skrede, O.-J., De Raedt, S., Kleppe, A., Hveem, T. S., Liestøl, K., Maddison, J., Askautrud, H. A., Pradhan, M., Nesheim, J. A., Albrechtsen, F. et al. (2020). Deep learning for prediction of colorectal cancer outcome: a discovery and validation study. *The Lancet*, *395*, 350–360.
- Tan, M., Pang, R., & Le, Q. V. (2020). Efficientdet: Scalable and efficient object detection. In *Proceedings of the IEEE/CVF conference on computer vision and pattern recognition* (pp. 10781–10790).
- Team, N. L. S. T. R. (2011). The national lung screening trial: overview and study design. *Radiology*, *258*, 243–53. doi:<https://doi.org/10.1148/radiol.10091808>.
- Vaswani, A., Shazeer, N., Parmar, N., Uszkoreit, J., Jones, L., Gomez, A. N., Kaiser, Ł., & Polosukhin, I. (2017). Attention is all you need. *Advances in neural information processing systems*, *30*.
- Wang, W., Xie, E., Li, X., Fan, D.-P., Song, K., Liang, D., Lu, T., Luo, P., & Shao, L. (2021). Pyramid vision transformer: A versatile backbone for dense prediction without convolutions. In *Proceedings of the IEEE/CVF International Conference on Computer Vision* (pp. 568–578).
- Wang, X., Yan, Y., Tang, P., Bai, X., & Liu, W. (2018). Revisiting multiple instance neural networks. *Pattern Recognition*, *74*, 15–24.
- Yao, J., Zhu, X., Jonnagaddala, J., Hawkins, N., & Huang, J. (2020). Whole slide images based cancer survival prediction using attention guided deep multiple instance learning networks. *Medical Image Analysis*, *65*, 101789.
- Yu, K.-H., Zhang, C., Berry, G. J., Altman, R. B., Ré, C., Rubin, D. L., & Snyder, M. (2016). Predicting non-small cell lung cancer prognosis by fully automated microscopic pathology image features. *Nature communications*, *7*, 1–10.
- Zadeh, S. G., & Schmid, M. (2021). Bias in cross-entropy-based training of

deep survival networks. *IEEE Transactions on Pattern Analysis and Machine Intelligence*, 43, 3126–3137. doi:10.1109/TPAMI.2020.2979450.

Zaheer, M., Kottur, S., Ravanbakhsh, S., Poczos, B., Salakhutdinov, R. R., & Smola, A. J. (2017). Deep sets. *Advances in neural information processing systems*, 30.

Zarella, M. D., Bowman, D., Aeffner, F., Farahani, N., Xthona, A., Absar, S. F., Parwani, A., Bui, M., & Hartman, D. J. (2018). A Practical Guide to Whole Slide Imaging: A White Paper From the Digital Pathology Association. *Archives of Pathology & Laboratory Medicine*, 143, 222–234. doi:10.5858/arpa.2018-0343-RA.

Zeiler, M. D., & Fergus, R. (2014). Visualizing and understanding convolutional networks. In *European conference on computer vision* (pp. 818–833). Springer.

Zeiser, F. A., da Costa, C. A., de Oliveira Ramos, G., Bohn, H. C., Santos, I., & Roehe, A. V. (2021). Deepbatch: A hybrid deep learning model for interpretable diagnosis of breast cancer in whole-slide images. *Expert Systems with Applications*, 185, 115586. doi:https://doi.org/10.1016/j.eswa.2021.115586.

Zhang, D., Zhang, H., Tang, J., Wang, M., Hua, X., & Sun, Q. (2020). Feature pyramid transformer. In *European Conference on Computer Vision* (pp. 323–339). Springer.

Zhang, H., Meng, Y., Zhao, Y., Qiao, Y., Yang, X., Coupland, S. E., & Zheng, Y. (2022). Dtf-d-mil: Double-tier feature distillation multiple instance learning for histopathology whole slide image classification. In *Proceedings of the IEEE Conference on Computer Vision and Pattern Recognition* (pp. 18802–18812).

Zhou, B., Khosla, A., Lapedriza, A., Oliva, A., & Torralba, A. (2016). Learning deep features for discriminative localization. In *Proceedings of the IEEE conference on computer vision and pattern recognition* (pp. 2921–2929).

Zhu, X., Yao, J., Zhu, F., & Huang, J. (2017). Wsisa: Making survival prediction from whole slide histopathological images. In *Proceedings of the IEEE Conference on Computer Vision and Pattern Recognition* (pp. 7234–7242).